

Multimode Entangled Squeezed Light Generation and Propagation in a Coupled-Cavity Photonic Crystal

Dylan van Eeden* and Marc M. Dignam

*Department of Physics, Engineering Physics, and Astronomy
Queen's University, Kingston, Ontario K7L 3N6, Canada*

(Dated: April 30, 2025)

We present an efficient and accurate method for modeling the generation and propagation of quantum states of light in lossy coupled-cavity systems. We apply our approach to the design and modeling of a multimode photonic crystal coupled-cavity system for the generation of entangled squeezed states of light on-chip. The system consists of a three-mode, three-defect resonant structure coupled to three coupled-resonator optical waveguides (CROWs) in a square lattice silicon photonic crystal slab. We model the system using a basis of 184 non-orthogonal lossy quasi-modes. A two-mode squeezed thermal state of light is generated via degenerate spontaneous four-wave mixing in the resonant structure, which is pumped with a Gaussian pulse via a pump-CROW. The generated entangled signal and idler pulses of light are coupled out of the resonant structure into the two output-CROWs. Due to careful design of the resonant structure and the CROWs, the signal and idler light in the two output CROWs remains entangled even after propagating tens of cavities down the CROWs. Our approach is general and computationally efficient and thus can be applied to modeling the generation and propagation of quantum states of light in a wide variety of coupled-cavity photonic structures.

I. INTRODUCTION

Entangled squeezed thermal states of light [1, 2] are sought for their entanglement and noise properties. They lend themselves to applications such as continuous-variable quantum computing [3–5], quantum key distribution [6], quantum-enhanced sensing [7–9], and the generation of non-Gaussian entangled states of light [10]. Consequently, there is considerable interest in developing and modeling nanophotonic platforms for the generation of entangled quantum states of light.

Entangled, multi-mode, squeezed thermal states of light may be created by generating single-mode squeezed thermal states of light in an optical cavity [11, 12] and interfering them using a beam-splitter array to build multi-mode entanglement [13]. Alternatively, they can be generated directly via a nonlinear process described by a Hamiltonian containing terms with an operator of the form $(a_1^\dagger a_2^\dagger)^n$, $n \in \mathbb{N}^{>0}$,

where a_i^\dagger is the creation operator for photons in the i^{th} mode.

Nonlinear devices using microring resonators have been explored both experimentally [13–16] and theoretically [12, 17–22] for the generation of entangled squeezed states of light. Photonic crystal (PC) coupled cavity systems (CCSs) have also been investigated theoretically [23–25] for the generation of squeezed states of light.

Microring resonator systems can be fabricated with very high quality factors (Q) [16] and are relatively simple to design, fabricate, and couple to channel waveguides. However, they support a large number of nearly equally spaced modes, which can lead to parasitic nonlinear processes that degrade the properties of the desired quantum state [16, 26]. In contrast, although the quality factors of the resonant modes in PC CCSs are generally an order of magnitude or more smaller than can be attained in microrings, the resonant cavities are much smaller, with cavity sizes on the order of hundreds of nanometers. Moreover, they can be designed such that they only support the modes required for the desired optical processes.

* dylan.vaneeden@queensu.ca

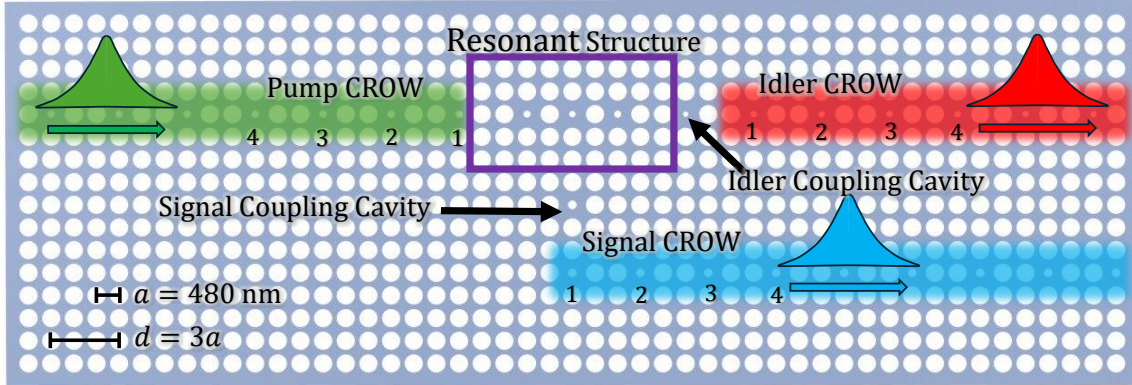


FIG. 1: Schematic of the designed photonic crystal coupled-cavity system in the vicinity of the resonant structure (outlined by the purple box) with key features highlighted. White regions indicate air holes etched into the silicon slab (pale blue). A pump pulse is injected via the pump CROW (green, left of RS), and the generated light leaves the RS via the signal (blue, lower-right of RS) and idler (red, right of RS) CROWs in spatially separated pulses. The numbers below the three CROWs, indicate the cavity labeling convention that will be used in Sec. IV. Note that the three CROWs used in the simulation are much longer than shown here, with each containing over 50 coupled cavities.

In this work, we examine PC CCSs as an alternative platform to microring resonators (see Fig. 1). We exploit the ability to choose the number and frequency spacing of resonant-structure modes and to tailor the pass-band of coupled resonator optical waveguides (CROWs) to design a PC CCS to generate and propagate two-mode entangled squeezed states of light. In addition, we use this system to demonstrate the effectiveness of our theoretical approach in simulating the generation of multi-photon quantum states of light in complicated dielectric nanostructures.

Any nanophotonic system used to generate entangled squeezed states, regardless of the mechanism of generation, is a complicated dielectric structure with multiple interacting elements. Such composite systems are difficult to model and simulate. Any theoretical framework employed must be able to model not only each individual element but also their mutual interactions and their loss to the environment. In this work, we present an approach to simulating the nonlinear generation of quan-

tum states of light in systems of coupled lossy nanophotonic resonators in which there is a localized region – the *resonant structure* (RS) – where the nonlinear interaction occurs. Our approach uses a basis of non-orthogonal, lossy quasi-modes (QMs) [27, 28] to account for the loss characteristic of the open resonators from which the system is constructed. We focus our attention on a PC CCS in this work, but our method can be applied to other nanophotonic resonator systems.

Our theoretical and computational approach involves four distinct steps. First, we determine the QMs of the full system under consideration. To accomplish this, we use finite difference time domain (FDTD) simulations to compute the electric field profile and quality factor of the QMs of the single-defect cavities from which we construct the PC CCS [29]; we then use a tight-binding approach to construct the QMs of the full system from these single-defect modes [27–30]. Second, we use this basis of system QMs to compute the classical evolution of the pump light (for a given initial pump field)

and determine the pumping-field amplitude inside the RS as a function of time. Third, we compute the time evolution of density operator of the quantum state of light generated via nonlinear interaction in the RS. Fourth, we solve the Lindblad master equation after the pump has peaked in order to determine the quantum evolution of the generated state throughout the system.

To demonstrate our approach, we design and simulate a PC CCS capable of generating two-mode entangled squeezed thermal states directly. The system consists of a three-mode, three-defect RS coupled to three CROWs [31] in a square lattice silicon photonic crystal slab (see Fig. 1). The PC CCS we propose is a spatially smaller alternative to the microring resonator-based systems [14–16, 21, 26]. The entangled two-mode squeezed thermal state is generated in the RS at the signal and idler frequencies via spontaneous four-wave mixing (SFWM) when excited by a Gaussian pump pulse at the pump frequency, which is midway between the signal and idler frequencies. The key element of the system is the RS, which is comprised of three single-defect cavities and supports three resonant modes, one each at the signal, pump, and idler frequencies. The RS enhances the nonlinear spontaneous four wave mixing process that generates the desired entangled state. The generated light propagates out of the RS as two entangled pulses at the signal and idler frequencies in spatially-distinct CROWs that are designed to block any pump light.

The paper is organized as follows: in Section II, we provide a detailed description of the designed device and outline the design goals; in Section III, we introduce the four-step analysis procedure we developed to simulate the designed system; in Section IV, we present and discuss the results of the analysis; and finally in Section V, we present our conclusions.

II. SYSTEM OVERVIEW AND DESIGN GOALS

In this section, we describe the PC CCS that we have designed and optimized using our theoretical approach. We present our design process, outline the objectives of our design, and present the specifications of the designed PC CCS within which we will simulate the generation and propagation of multimode squeezed light.

The structure is a PC CCS with a three-mode RS and three CROWs in a PC slab, shown schematically in Fig. 1. The underlying PC slab is a 384 nm thick silicon ($n=3.47$) slab with air holes of radius 192 nm etched in a rectangular lattice with a lattice constant $a = 480$ nm. This particular square lattice geometry of the PC was chosen because the single-defect cavities formed in this PC support a single relatively high-Q mode in the photonic band-gap of the PC [29].

We have designed the structure to generate and propagate entangled two-mode (2M) squeezed thermal states (STS) with high brightness and robust entanglement. We have four main objectives for the design of the PC CCS. First, we need a RS with spatially-overlapping modes at the frequencies of the pump (ω_P), signal (ω_S), and idler (ω_I), where $2\omega_P = \omega_S + \omega_I$ so that the process of SFWM can result in the generation of a quantum state of light in the signal and idler modes. Second, we need to be able to inject the pump light into the RS via a CROW such that there is a large pump intensity buildup inside of the RS. Third, we require that the quantum state of light generated in the RS can couple out of the RS into two separate CROWs, with central frequencies, ω_s and ω_I , that do not allow propagation of the pump light.

The CCS was designed starting with the RS, outlined in solid purple in Fig. 1. The RS contains three cavities: the outer two have air holes with radii of 74 nm and the center has an air hole with a radius of 80 nm. This three-cavity structure supports three resonant QMs, with frequencies of $\omega_I = 0.30610 \ 2\pi c/a$,

$\omega_P = 0.30763 \ 2\pi c/a$, $\omega_S = 0.30916 \ 2\pi c/a$, corresponding to the following wavelengths in the telecom band: $\lambda_I \approx 1568 \text{ nm}$, $\lambda_P \approx 1560 \text{ nm}$, $\lambda_S \approx 1553 \text{ nm}$. We selected this particular configuration to satisfy the condition $2\omega_P = \omega_I + \omega_S$ to within 0.002 percent. We will explore the characteristics of the RS further in Sec. III.

The three CROWs were designed such that their bandwidths encompass only one of the pump, signal, or idler frequencies. This is achieved by constructing each CROW from a single-defect cavity with a resonant frequency equal to the frequency of the corresponding mode of the RS, ω_I , ω_P , and ω_S for the idler, pump, and signal CROWs respectively. The resultant single-defect cavities chosen have radii of 66, 76, and 89 nm respectively for the idler, pump, and signal CROWs. All three CROWs have a period $d = 3a$. The dispersion curves for the three CROWs are shown in Fig. 2.

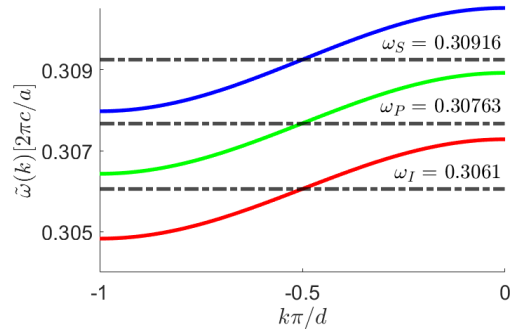


FIG. 2: Dispersion for the CROW bands as calculated in the nearest-neighbor tight-binding approximation (see Sec. III A 3). Idler, pump, and signal CROW bands are shown in red, green, and blue, respectively, with corresponding RS QM frequencies displayed as dashed lines intersecting their corresponding CROW band.

Note that the resonant frequencies are at the center of each CROW band and that ω_S and ω_I lie outside the pump band. Thus, the pump light does not contaminate the output light in the two other CROWs. As we shall discuss in Section III, the generated light will exit the reso-

nant structure via the signal and idler CROWs. Because the signal and idler bands do not overlap, there will be no cross-contamination of the signal and idler modes at the output. The band-pass filtering functionality is one of the reasons that we have used CROWs rather than line-defect waveguides to couple the light into and out of the RS. The key properties of the system are summarized in Table I.

Parameter	Pump	Signal	Idler
RS QM λ [nm]	1560	1553	1568
RS QM f [THz]	192.1	193.1	191.2
RS QM ω [$2\pi c/a$]	0.3076	0.3092	0.3061
RS QM intrinsic Q	18800	41900	12900
CROW Cav. Rad. [nm]	76	89	66
CROW Ctr. Freq. [THz]	192.3	193.2	191.2
Coupling Cav. Rad. [nm]	-	91	55

TABLE I: Summary of RS QM properties, defect cavity radii, and CROW properties for the PC CCS shown in Fig. 1.

III. THEORETICAL APPROACH

In this section, we present our theoretical approach to simulating the generation of quantum states of light via nonlinear processes in a PC CCS.

Our approach can be broken into four distinct steps, shown pictorially in Fig. 3. Before presenting detailed discussions of each of the steps, we start with an overview of each of the steps.

First, we calculate the four different bases to be used in the simulation: the single-defect QMs, the Bloch QMs of the pump CROW, the RS QMs, and the full-system QMs. To accomplish this, we first compute the QMs of the individual cavities using FDTD calculations. We then use the QMs of the individual cavities in a tight-binding approach to calculate the QMs of the different subsystems and the entire system.

Second, we calculate the classical evolution of the pump pulse as it propagates along the pump CROW and couples into the RS. In this step we begin the analysis by describing the pump pulse

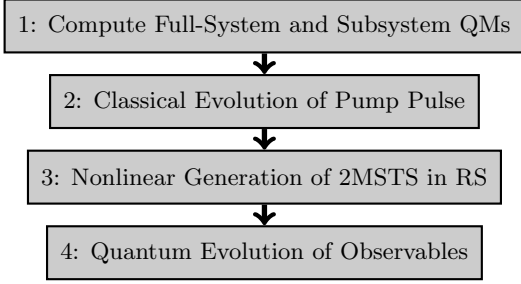


FIG. 3: Procedure flowchart for the four-step analysis used to calculate the quantum state of light in the output CROWS.

at the initial time in the basis of Bloch modes of an infinite version of the pump CROW. We next project this pulse onto the basis of single-defect modes in the CROW. We then project onto the full-system QMs, which allows to determine the time-evolution of the pump. We finally project the time-evolved pump field onto the basis RS QMs to compute the pump amplitude in the RS, which will be used in the next step.

Third, we numerically solve a system of coupled differential equations to compute the parameters of the entangled two-mode squeezed thermal state generated in the RS from the pump pulse. These differential equations contain a driving term proportional to the square of the pump amplitude in the RS we calculated in the prior step. We model the generation process in the basis of RS QMs.

Fourth, we take the density operator calculated in step three at the time where the two-mode squeezing has peaked to be the initial quantum state of the generated light. At this time, the pump pulse in the RS is weak, and so we make the conservative approximation that it is absent at later times. This allows us to calculate the free quantum evolution of the generated light in the full structure

We now discuss each step of our theoretical approach in detail.

A. Coupled-Cavity System QMs

As our first step, we calculate the QMs of the individual defects and present the tight-binding formalism that we use to obtain the leaky QMs of the entire PC CCS discussed earlier and shown in Fig. 1. We first discuss some general properties of PC slabs and defect modes, and then show how we determine the QMs of a general system of coupled defects. We then compute the QMs of the full system and each of the subsystems.

1. General Procedure

Defect-free PC slabs are periodic dielectric structures which, if properly designed, can support a photonic band gap - a set of frequencies for which light cannot propagate in the PC - similar to an electronic band gap in which no electronic states exist [32]. Both of these band gaps arise from the periodicity of the underlying structure. The photonic band structure (and thus the size and location of the photonic band gap) of a PC slab is easily calculated using finite-difference time-domain (FDTD) simulations or finite-element analysis (FEA) by exploiting the high symmetry in a defect-free PC slab.

One may form *single-defect cavities* in a PC slab by removing or shrinking an air hole at a particular lattice site, and thus locally disrupting the periodicity of the structure. Defects of this type are displayed in Fig. 1. These single-defect cavities in a square-lattice PC slab support a quadrupole-like resonant QM localized to the lattice site of the altered air hole [29]. The resonant frequency of the single-defect cavity modes formed in this manner lies within the transverse electric photonic band gap of the underlying PC slab.

In principle, one could obtain the QMs of a system of coupled defects via FDTD or FEA, though achieving accurate results from these simulations becomes prohibitively resource-intensive as the number of defects increases, especially if the system has low sym-

metry and the modes are close together in frequency relative to their intrinsic linewidth. Instead, we obtain the system QMs through a tight-binding expansion of the system QMs in terms of the (lossy) QMs of the individual defects that comprise the PC CCS.

The positive frequency part of the electric field of light in the q^{th} individual defect QM is given by [30]

$$\mathbf{E}_q^+(\mathbf{r}, t) = \sqrt{\frac{\hbar\Omega_q}{2\epsilon_0}} \mathbf{M}_q(\mathbf{r}) e^{-i\tilde{\Omega}_q t}, \quad (1)$$

where $\mathbf{M}_q(\mathbf{r})$ is the spatial profile of the leaky resonant mode supported by the q^{th} cavity. These QMs are subject to normalization condition

$$\int d^3\mathbf{r} \epsilon_p(\mathbf{r}) \mathbf{M}_p^*(\mathbf{r}) \cdot \mathbf{M}_p(\mathbf{r}) = 1, \quad (2)$$

and satisfy the Helmholtz equation

$$\nabla \times \nabla \times \mathbf{M}_q(\mathbf{r}) - \frac{\tilde{\Omega}_q^2}{c^2} \epsilon_q(\mathbf{r}) \mathbf{M}_q(\mathbf{r}) = 0, \quad (3)$$

where $\epsilon_q(\mathbf{r})$ is the dielectric function of the PC containing only the q^{th} defect and $\tilde{\Omega}_q = \Omega_q - i\gamma_q$ is the complex frequency of the mode in the q^{th} cavity. We obtain these QMs and their complex frequencies via FDTD simulations. These modes are inherently lossy, with the effects of loss captured by the complex nature of the system QM frequencies: the real part, Ω_q , gives the resonant frequency and the imaginary part, γ_q , describes the energy leakage out of the q^{th} defect mode. The quality factor of the mode is given simply by $Q_q = \Omega_q/2\gamma_q$.

In Fig. 4, we plot the resonant frequency and quality factor of a single-defect cavity as a function of defect-hole radius. Note that by changing the hole radius from 50 nm to 150 nm, we can tune the resonant frequency by about 7%, while the quality factor ranges from about 14,500 to about 20,500. This tunability allows us to design the RS, the CROWS, and the coupling cavities to achieve our overall design goals.

The $\mathbf{M}_q(\mathbf{r})$ act as a basis for full system QMs that have frequencies well inside the chosen band gap of the PC. We use a tight-binding

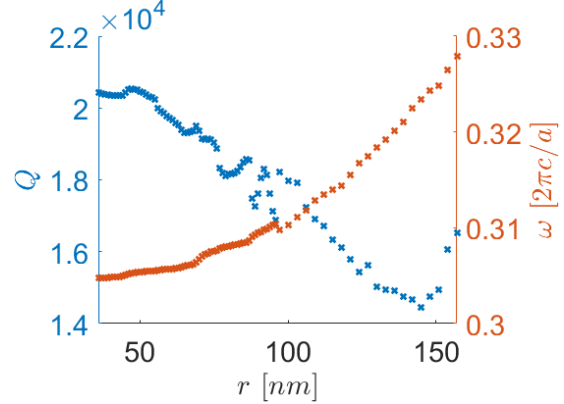


FIG. 4: Single-defect QM frequency and quality factor as a function of defect air hole radius for the chosen PC. Computed with ANSYS Lumerical FDTD [33].

approach and expand the system QMs, $\mathbf{N}_\mu(\mathbf{r})$, in terms these as [27]

$$\mathbf{N}_\mu(\mathbf{r}) = \sum_q v_{q\mu} \mathbf{M}_q(\mathbf{r}), \quad (4)$$

where the $v_{q\mu}$ are the expansion coefficients for the μ^{th} system QM. The positive-frequency part of the electric field in the μ^{th} system QM then takes the form

$$\mathbf{E}_\mu^+(\mathbf{r}, t) = \sqrt{\frac{\hbar\omega_\mu}{2\epsilon_0}} \mathbf{N}_\mu(\mathbf{r}) e^{-i\tilde{\omega}_\mu t}, \quad (5)$$

where $\tilde{\omega}_\mu = \omega_\mu - i\gamma_\mu$ is the complex frequency of the μ^{th} system QM. The $\mathbf{N}_\mu(\mathbf{r})$ satisfy the Helmholtz equation

$$\nabla \times \nabla \times \mathbf{N}_\mu(\mathbf{r}) - \frac{\tilde{\omega}_\mu^2}{c^2} \epsilon(\mathbf{r}) \mathbf{N}_\mu(\mathbf{r}) = 0, \quad (6)$$

where $\epsilon(\mathbf{r})$ is the dielectric function of the full system.

Eqs. (3), (4), and (6) lead to the generalized eigenvalue problem [27]

$$\overleftrightarrow{\Lambda} \overleftrightarrow{\Omega} \overleftrightarrow{V} = \overleftrightarrow{\Lambda} \overleftrightarrow{B} \overleftrightarrow{V}, \quad (7)$$

where $\overleftrightarrow{\Omega} \equiv \text{Diag}(\tilde{\Omega}_q^2)$, $\overleftrightarrow{\Lambda} \equiv \text{Diag}(\tilde{\omega}_\mu^2)$, \overleftrightarrow{V} is a square matrix whose elements are the $v_{q\mu}$ from

Eq. (4), and \overleftrightarrow{A} and \overleftrightarrow{B} are respectively the overlap and coupling matrices for the coupled-cavity structure, whose elements are defined as:

$$A_{pq} = \int d^3\mathbf{r} \epsilon_p(\mathbf{r}) \mathbf{M}_p^*(\mathbf{r}) \cdot \mathbf{M}_q(\mathbf{r}), \quad (8)$$

$$B_{pq} = \int d^3\mathbf{r} \epsilon(\mathbf{r}) \mathbf{M}_p^*(\mathbf{r}) \cdot \mathbf{M}_q(\mathbf{r}). \quad (9)$$

Note that all independent quantities in Eqs. (7)-(9) can be obtained from FDTD/FEA simulations of individual defects. The number of required FDTD simulations is equal to the number of unique cavities, rather than the number of total cavities. In the designed system, there are 184 total cavities, but only 7 unique cavities. We will use the full-system QMs $\mathbf{N}_\mu(\mathbf{r})$ as a basis for the classical time evolution of the pump field and the quantum evolution of the generated light.

The inner product between the system QMs is defined as

$$\langle \mathbf{N}_\mu | \mathbf{N}_\nu \rangle \equiv \int_\infty d^3\mathbf{r} \epsilon(\mathbf{r}) \mathbf{N}_\mu^*(\mathbf{r}) \cdot \mathbf{N}_\nu(\mathbf{r}) \quad (10)$$

$$= V_\mu^\dagger \overleftrightarrow{B} V_\nu \quad (11)$$

$$= O_{\mu\nu}, \quad (12)$$

where V_μ is the μ^{th} column of \overleftrightarrow{V} . The $O_{\mu\nu}$ are elements of the square Hermitian matrix \mathbf{O} , called the QM overlap matrix. Note that although they are chosen to be normalized ($O_{\mu\mu} = 1 \forall \mu$), *the full system QMs are not orthogonal*. This is due to the loss in the system, which makes the problem non-Hermitian [29, 30]. In Fig. 5 we plot the overlaps between all of the 184 full-system QMs, as computed with Eq. (12). It is immediately apparent that a significant number of QM pairs are far from being orthogonal. In particular, some of the QMs that are very close in frequency have overlaps that are significantly more than 0.1.

The non-orthogonality of the full-system QMs needs to be accounted for in the commutation relations of the system QM creation and annihilation operators. As we will show in Sec. III, the effect of the overlap matrix mathematically is to mix the QMs during the free evolution

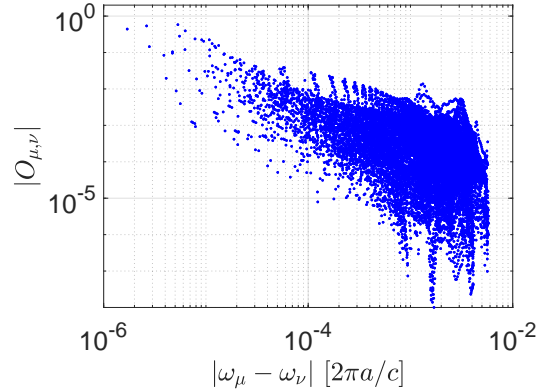


FIG. 5: Absolute values of the QM overlaps $O_{\mu,\nu}$ for the full system as a function of the absolute value of frequency difference between the μ and ν QMs.

of the light. This mixing will have non-trivial effects on the dynamics of the system and cannot be ignored. We will address the consequences of the non-orthogonality in detail in Sec. IV. We now proceed with the computation of the QMs in each of the *subsystems*.

2. Resonant Structure Quasi-Modes

The first subsystem that we focus on is the RS. The RS QMs are computed in the same manner as those of the full structure, but we only include the cavities comprising the RS when calculating these QMs. The positive frequency part of light in the j^{th} RS QM takes the form

$$\mathbf{E}_j^+(\mathbf{r}, t) = i \sqrt{\frac{\hbar \omega_j}{2\epsilon_0}} \mathbf{C}_j(\mathbf{r}) e^{-i\tilde{\omega}_j t}, \quad (13)$$

where $\mathbf{C}_j(\mathbf{r})$ is j^{th} QM ($j = \{I, P, S\}$) of the RS and $\tilde{\omega}_j \equiv \omega_j - i\gamma_j$ is its complex frequency. The $\mathbf{C}_j(\mathbf{r})$ satisfy the Helmholtz equation

$$\nabla \times \nabla \times \mathbf{C}_j(\mathbf{r}) - \frac{\tilde{\omega}_j^2}{c^2} \epsilon_{\text{RS}}(\mathbf{r}) \mathbf{C}_j(\mathbf{r}) = 0, \quad (14)$$

where $\epsilon_{\text{RS}}(\mathbf{r})$ is the dielectric function of the slab with only the RS defects present.

In this case the RS is constructed from three single-defect cavities arranged in a line (see Fig. 1). Following Section III A 1, the tight-binding eigenvalue problem for the RS QMs is

$$\overset{\leftrightarrow}{A}_{\text{RS}}\overset{\leftrightarrow}{\Omega}_{\text{RS}}\overset{\leftrightarrow}{U} = \overset{\leftrightarrow}{\Lambda}_{\text{RS}}\overset{\leftrightarrow}{B}_{\text{RS}}\overset{\leftrightarrow}{U}, \quad (15)$$

where $\overset{\leftrightarrow}{A}_{\text{RS}}$ and $\overset{\leftrightarrow}{B}_{\text{RS}}$ have elements respectively given by Eqs. (8) and (9) with $\epsilon \rightarrow \epsilon_{\text{RS}}$ and the elements, u_{qj} of $\overset{\leftrightarrow}{U}$ are the expansion coefficients of the RS QMs according to

$$\mathbf{C}_j(\mathbf{r}) = \sum_q u_{qj} \mathbf{M}_q(\mathbf{r}), \quad (16)$$

where the sum is only over the three defect modes in the RS.

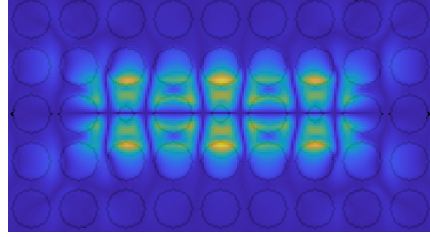
In Fig. 6, we plot $|C_{j,x}(x, y, 0)|^2$ for each of the three RS QMs and list their complex frequencies. We can see that the three RS QMs strongly overlap in space. The real parts of the frequencies of the RS QMs dictate the operating frequencies for SFWM. The band structures of the CROWs plotted in Fig. 2 are designed to center on the RS QM frequencies. The hole sizes of the defects used to arrive at the final frequency configuration were chosen by comparing the computed QMs of combinations of three defect configurations in which the wing cavities were identical.

3. Bloch Modes of an Infinite CROW

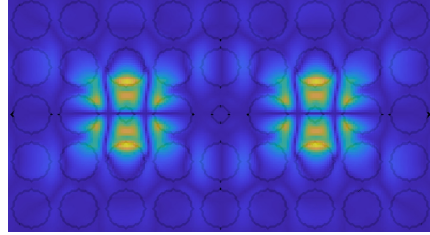
The remaining subsystems are the three CROWs. To understand the modes of the finite CROWS in the system, it is useful to first determine the Bloch QMs of infinite CROWs. In the nearest-neighbor tight-binding (NNTB) approximation, these modes can be expanded in the basis of single-defect cavity QMs as [27]

$$\mathbf{F}_k(\mathbf{r}) = \frac{1}{\sqrt{N}} \sum_q e^{ikqd} \mathbf{M}_q(\mathbf{r}), \quad (17)$$

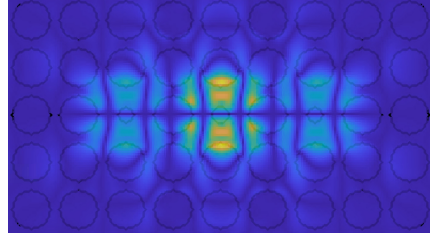
where $d = 3a$ is the CROW period and N is the number of cavities in the CROW, which is



(a) Idler, $\tilde{\omega}_I = 0.30610 - i1.19 \times 10^{-5} 2\pi c/a$



(b) Pump, $\tilde{\omega}_P = 0.30763 - i8.17 \times 10^{-6} 2\pi c/a$



(c) Signal, $\tilde{\omega}_S = 0.30916 - i3.69 \times 10^{-6} 2\pi c/a$

FIG. 6: Plot of $|C_{j,x}(x, y, 0)|^2$ for the three RS QMs. The area of each subfigure is enclosed by the purple rectangle in Fig. 1. The color scale is linear, with bright yellow indicating the peak value and dark blue indicating zero. The complex frequency for each of the QMs (when the CROWs are absent) are given below each plot.

taken to be of length $L = Nd$. In the limit that $N \rightarrow \infty$, the solution to the generalized eigenvalue problem for the CROW in the NNTB gives [25]

$$\tilde{\omega}_k = \tilde{\Omega}_0 [1 + (A_{01} - B_{01}) \cos(kd)], \quad (18)$$

for the complex frequency of the Bloch mode with Bloch wavevector k , where $\tilde{\Omega}_0$ is the complex frequency of all of the identical single cav-

ity modes in the CROW and A_{01} and B_{01} are overlaps given in Eqs. (8) and (9) for neighboring single-cavity modes in the CROW structures. The radius of the defect holes in a given CROW is chosen to match the center frequency of that CROW band to the frequency of the corresponding RS QM (P, S, I). In Fig. 2, we plot the real part of the CROW frequencies as a function of the Bloch wavenumber, k , for all three CROWs.

The decay rate of light out of the resonant structure into the three CROWs is controlled by two *coupling cavities* located between the resonant structure and the signal and idler CROWs (see Fig. 1). The signal and idler coupling cavities have air hole radii of 55 and 91 nm respectively. As we shall discuss in more detail in Section III, these cavities tune the coupling between the resonant structure and the signal and idler CROWs. We have chosen the coupling cavities such that the loaded decay rates of the signal and idler RS QMs are similar. The objective is to strongly couple the signal and idler CROWs to the RS to allow entanglement to persist in the CROWs without compromising the nonlinear generation process.

B. Pump Evolution

Now that we have computed the various bases with which we will describe the light, we turn our attention to modeling the evolution of the pump light. The pump at time $t = 0$ starts in a coherent (classical) state in the pump CROW. We choose the initial state of the pump to be a Gaussian in the Bloch modes, centered at $k_0 = -\frac{\pi}{2d}$. With this choice, the propagation speed is maximized, there is no waveguide group velocity dispersion, and the frequency is centered at the pump frequency of the RS: $\omega_{k_0} = \Omega_0 = \omega_P$. Thus, the positive frequency part of the electric field of the pump light at time $t = 0$ is given by

$$\mathbf{E}_P^{(+)}(\mathbf{r}, t = 0) = i \sum_k \alpha_P^{(0)}(k) \sqrt{\frac{\hbar \tilde{\omega}_k}{2\epsilon_0}} \mathbf{F}_k(\mathbf{r}), \quad (19)$$

where the $\alpha_P^{(0)}(k)$ are the expansion coefficients, which take the form

$$\alpha_P^{(0)}(k) = \sqrt{\frac{\kappa d n_p}{\sqrt{2\pi}}} e^{-(k-k_0)^2/\kappa^2} e^{-iq_0 k d}, \quad (20)$$

where n_p is the total number of photons initially in the pump pulse, q_0 is the cavity on which the pulse is centered at $t = 0$, and κ is the k -space width parameter of the pulse.

Using Eq. (20) in Eq. (19) and evaluating the sum over k in the limit that N is very large, we obtain after some work

$$\mathbf{E}_P^+(\mathbf{r}, 0) = i \sqrt{\frac{\hbar \omega_P}{2\epsilon_0}} \sum_{q=1}^N x_q \mathbf{M}_q(\mathbf{r}), \quad (21)$$

where

$$x_q = \sqrt{\frac{\kappa d n_p}{\sqrt{2\pi}}} e^{-\kappa^2 d^2 (q-q_0)^2/4} e^{i(q-q_0)k_0 d}. \quad (22)$$

Now, to determine the time evolution of the pump in the full system, we need to expand the pump field at $t = 0$ in terms of the QMs of the full system, since we know that these evolve in time according to Eq. (5). We start by inverting Eq. (4) to obtain the single cavity modes in terms of the modes of the full system:

$$\mathbf{M}_q(\mathbf{r}) = \sum_{\mu} w_{\mu q} \mathbf{N}_{\mu}(\mathbf{r}), \quad (23)$$

where $w_{\mu q}$ are the elements of $\overset{\leftrightarrow}{W} = \overset{\leftrightarrow}{V}^{-1}$. Using this in Eq. (21) and using Eq. (22), we obtain

$$\mathbf{E}_P^+(\mathbf{r}, t) = i \sqrt{\frac{\hbar \omega_P}{2\epsilon_0}} \sum_{q=1}^N x_q \sum_{\mu} w_{\mu q} \mathbf{N}_{\mu}(\mathbf{r}) e^{-i\tilde{\omega}_{\mu} t}. \quad (24)$$

Finally, using Eq. (4) to express the full system modes once again in terms of the cavity modes, we obtain

$$\mathbf{E}_P^+(\mathbf{r}, t) = i \sqrt{\frac{\hbar \omega_P}{2\epsilon_0}} \sum_{p=1}^N y_p(t) \mathbf{M}_p(\mathbf{r}), \quad (25)$$

where

$$y_p(t) \equiv \sum_q x_q \sum_\mu w_{\mu q} v_{p\mu} e^{-i\tilde{\omega}_\mu t}. \quad (26)$$

Eqs. (22), (25), and (26) may be used to reconstruct the electric field of the pump in the full structure as a function of time.

C. Nonlinear Generation

In this section, we present our approach to calculating the density operator of the two-mode squeezed thermal state generated in the RS of our system via SFWM. We make the undepleted pump approximation, *i.e.*, we assume that the pump is unaffected by the nonlinear interaction. This is a good approximation as long as the number of photons generated is much less than the number of photons in the pump in the RS, which (as we shall show) is the case in our simulations. We shall label the ladder operators for the q^{th} single-defect cavity mode as $\{a_q, a_q^\dagger\}$. Restricting ourselves to the three modes of the RS, we define the ladder operators, $\{d_j, d_j^\dagger\}$, for the j^{th} RS QM in terms of the single-defect QM ladder operators as:

$$d_j = \sum_{q=1}^3 u_{qj} a_q, \quad d_j^\dagger = \sum_{q=1}^3 u_{qj}^* a_q^\dagger. \quad (27)$$

In this work, we only consider the SFWM nonlinear interaction in which two pump photons are exchanged for one signal and one idler photon. The Hamiltonian for the SFWM process is given by [11, 23]

$$H^{\text{RS}} = H_L^{\text{RS}} + H_{\text{NL}}^{\text{RS}}, \quad (28)$$

where

$$H_L^{\text{RS}} = \sum_{j=I,P,S} \hbar\omega_j d_j^\dagger d_j, \quad (29)$$

is the linear part of the Hamiltonian and

$$H_{\text{NL}}^{\text{RS}} = \hbar\chi_{\text{eff}} \alpha_P^2(t) d_S^\dagger d_I^\dagger + h.c., \quad (30)$$

is the nonlinear part [12, 34], where $\alpha_P(t)$ is the dimensionless time-dependent coherent state amplitude of the pump *in the pump mode of the RS*,

$$\begin{aligned} \chi_{\text{eff}} &\equiv -\frac{9\hbar}{16\epsilon_0} \sqrt{\omega_P^2 \omega_S \omega_I} \\ &\times \sum_{i,j,k,l=1}^3 \int d^3\mathbf{r} \chi_{ijkl}^{(3)}(\mathbf{r}) \epsilon_{\text{RS}}(\mathbf{r}) \\ &\times C_{P,i}(\mathbf{r}) C_{P,j}(\mathbf{r}) C_{S,k}^*(\mathbf{r}) C_{I,l}^*(\mathbf{r}), \end{aligned} \quad (31)$$

is the effective nonlinear parameter carrying the dimensions of a rate, and $\chi_{ijkl}^{(3)}$ are the elements of the third-order nonlinear susceptibility tensor for the dielectric substrate, which is assumed to be homogeneous in the substrate and zero elsewhere. Using $\chi_{iiii}^{(3)} = 4n_2 n^2 \epsilon_0 c / 3$ with $n_2 = 4.5 \times 10^{-18} \text{ m}^2 \cdot \text{W}^{-1}$ for silicon at 1550 nm [35, 36], and setting all other components to zero, we find that $\chi_{\text{eff}} \approx (1.84 + 0.07i) \times 10^5 \text{ s}^{-1}$.

The time-dependent pump amplitude, $\alpha_P(t)$, is obtained by projecting $\mathbf{E}_P^+(\mathbf{r}, t)$ onto the pump QM of the RS [37]:

$$\begin{aligned} \alpha_P(t) &= -i \sqrt{\frac{2\epsilon_0}{\hbar\omega_P}} \int d^3\mathbf{r} \epsilon_{\text{RS}}(\mathbf{r}) \mathbf{C}_P^*(\mathbf{r}) \cdot \mathbf{E}_P^+(\mathbf{r}, t) \\ &\approx \sum_{q,q'} u_{qP}^* B_{qq'} y_{q'}(t). \end{aligned} \quad (32)$$

The dynamics of the generated light in the RS described by the Hamiltonian of Eq. (28) is obtained by solving the Lindblad master equation for the density operator projected onto the RS QMs, ρ^{RS} [28]. The Lindblad master equation takes the form [28]

$$\begin{aligned} \frac{d\rho^{\text{RS}}}{dt} &= -\frac{i}{\hbar} [H_L^{\text{RS}}, \rho^{\text{RS}}] \\ &+ i \sum_{j=I,S} \Gamma_j \left(d_j \rho^{\text{RS}} d_j^\dagger - \frac{1}{2} d_j^\dagger d_j \rho^{\text{RS}} - \frac{1}{2} \rho^{\text{RS}} b_j^\dagger b_j \right), \end{aligned} \quad (33)$$

where the Γ_j are the *loaded* power decay rates of the signal ($j = S$) and idler ($j = I$) modes (*i.e.*, the decay rates when the RS is coupled to all three CROWs), and we assume that the RS QMs are orthogonal, which is an excellent approximation for our RS ($|O_{SI}| \leq 0.01$).

Vendromin and Dignam have shown that the solution to Eq. (33) is the density operator of a two-mode STS [12], which takes the form

$$\rho^{RS} = S_2(\xi)\rho_{th}(t)S_2^\dagger(\xi), \quad (34)$$

where

$$\rho_{th}(t) \equiv \prod_{j=S,I} \left(\frac{1}{n_j^{\text{th}} + 1} \right) \left(\frac{n_j^{\text{th}}}{n_j^{\text{th}} + 1} \right)^{d_j^\dagger d_j} \quad (35)$$

is a two-mode thermal state with time-dependent thermal populations $n_j^{\text{th}}(t)$ and

$$S_2(\xi) = \exp\left(\xi^* d_S d_I - \xi d_S^\dagger d_I^\dagger\right) \quad (36)$$

is the two-mode squeezing operator with time-dependent squeezing parameter $\xi(t) = r(t)e^{i\theta(t)}$, where $r(t)$ is the squeezing amplitude and $\theta(t)$ is the squeezing phase.

Writing the nonlinear driving term as

$$\alpha_P^2(t)\chi_{\text{eff}} = |\alpha_P^2(t)\chi_{\text{eff}}|e^{-i\omega_P(t-t_0)}e^{i\beta(t)}, \quad (37)$$

we find, for our choice of initial pulse in the structure we have designed, that β is independent of t over the time range for which the pump is non-negligible. When β is independent of t and the initial state is the vacuum state, it can be shown that the squeezing phase evolves simply according to [12]

$$\theta(\tilde{t}) = -2\omega_P(\tilde{t} - \tilde{t}_0) - \frac{\pi}{2} + \beta, \quad (38)$$

and the squeezing amplitude and thermal photon numbers are governed by the following set of coupled first-order differential equations [12]:

$$\frac{dr}{d\tilde{t}} = \frac{g(\tilde{t})}{2} - \frac{\sinh(2r)}{n_S^{\text{th}} + n_I^{\text{th}} + 1} (1 + \zeta(n_I^{\text{th}} - n_S^{\text{th}})), \quad (39)$$

$$\begin{aligned} \frac{dn_S^{\text{th}}}{d\tilde{t}} &= n_S^{\text{th}}((1 - \zeta)\sinh^2 r - (1 + \zeta)\cosh^2 r) \\ &+ (1 - \zeta)\sinh^2 r, \end{aligned} \quad (40)$$

$$\begin{aligned} \frac{dn_I^{\text{th}}}{d\tilde{t}} &= n_I^{\text{th}}((1 + \zeta)\sinh^2 r - (1 - \zeta)\cosh^2 r) \\ &+ (1 + \zeta)\sinh^2 r, \end{aligned} \quad (41)$$

where we employ the dimensionless time units $\tilde{t} = \Gamma_+ t$ with $\Gamma_\pm = (\Gamma_S \pm \Gamma_I)/2$. The parameter $\zeta = \Gamma_-/\Gamma_+$, quantifies the difference in the loss rates in the two modes. Finally,

$$g(\tilde{t}) = \frac{2|\alpha_P^2(\tilde{t})\chi_{\text{eff}}|}{\Gamma_+} \quad (42)$$

is the pump strength in the pump mode. It is essentially the ratio of intensity buildup of the light in the pump mode to the decay rate of generated light, Γ_+ , out of the RS.

The Γ_j are computed by starting the system in a single-photon Fock state in one of the RS QMs, which we then expand in the basis of the full-system QMs. We then fit calculated time evolution of the photon number in the chosen RS QM to an exponential. From this procedure, we find that the loaded decay rate of the pump RS QM, which was not altered with a coupling cavity, is $\Gamma_P \approx 5.30 \times 10^{-5} 2\pi c/a$, and the intrinsic decay rate of the pump RS QM is $2\gamma_P \approx 1.63 \times 10^{-5} 2\pi c/a$. The loaded decay rates of the signal and idler RS QMs are $\Gamma_S \approx 2.58 \times 10^{-5}$ and $\Gamma_I \approx 2.6 \times 10^{-5} 2\pi/c$ respectively, while their intrinsic decay rates are $2\gamma_S \approx 7.37 \times 10^{-6}$ and $2\gamma_I \approx 2.38 \times 10^{-5} 2\pi c/a$ respectively. The loaded decay rates of the signal and idler RS QMs were tuned to be approximately equivalent and close to half the loaded decay rate of the pump RS QM. Tuning was accomplished by introducing a coupling cavity (labeled in Fig. 1) between the RS and each output CROW. These coupling cavities have the effect of decreasing the coupling between the RS and their respective CROWs - in this way, we decreased the couplings independently until they were at the desired values.

Eqs. (39-41) are solved numerically using a fourth-order Runge-Kutta method. In Fig. 7 (a), we plot the time evolution of the pump strength in the RS, $g(\tilde{t})$ (solid green), when a Gaussian pump pulse is initiated in the pump CROW with a pulse energy of 670 fJ, a center frequency at ω_P , and k -space width parameter $\kappa = 2\pi/20d$. For this pump, the peak number of pump photons in the RS is $\approx 2.3 \times 10^6$. In Fig. 7 (a), we also show the calculated time evolution of the total photon number in the signal (red

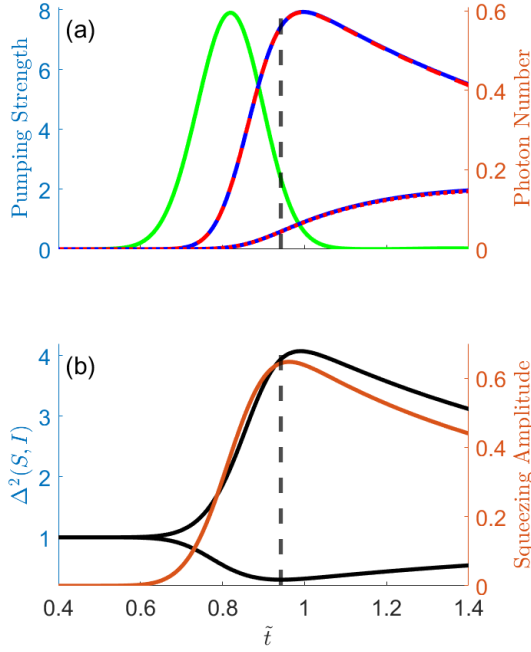


FIG. 7: Pump strength and numerical solutions to Eqs. (39-41) for a 6 pJ Gaussian pump pulse with a k -space width of $\kappa = 2\pi/20d$. (a) Pump strength $g(\tilde{t})$ (solid green, left axis) and photon number in the signal and idler RS QMs (right axis). The upper curves are the total photon number in the signal (blue, solid) and idler (red, dashed) RS QMs. The lower curves are the thermal photon numbers in the signal (blue, solid) and idler (red, dotted) RS QMs. Note that the results are almost identical for the signal and idler modes. (b) Squeezing amplitude (orange, right axis) and correlation variance envelope (black, left axis) between the signal and idler RS QMs.

dashed) and idler (blue solid) RS QMs, and the calculated thermal photon number in the signal (red dotted) and idler (blue solid) RS QMs. We see that most of the generated photons are contributing to squeezing rather than to thermal noise. We note that the expectation value of the photon number in the generated entangled

two-mode squeezed thermal state (2MSTS) is less than one, indicating the undepleted pump approximation is justified.

The correlation variance (CV) between the signal and idler RS QMs is defined as

$$\Delta_{S,I}^2 = \left\langle [\Delta(X_S - X_I)]^2 \right\rangle + \left\langle [\Delta(Y_S + Y_I)]^2 \right\rangle, \quad (43)$$

where

$$X_j = \frac{1}{2} (d_j e^{i\theta_j} + d_j^\dagger e^{-i\theta_j}), \quad (44)$$

$$Y_j = \frac{1}{2i} (d_j e^{i\theta_j} - d_j^\dagger e^{-i\theta_j}), \quad (45)$$

are the quadrature operators for the j^{th} RS QM. In these expressions, $\theta_S(t)$ and $\theta_I(t)$ are time dependent phases that can be chosen as desired. The correlation variance is an indicator of inseparability: if $\Delta_{S,I}^2 < 1$, then the state is entangled [38]. After substituting Eqs. (44, 45) into Eq. (43) we obtain

$$\Delta_{S,I}^2 = (n_S^{\text{th}} + n_I^{\text{th}} + 1) \times \{ \cosh(2r) + \cos(\theta_S + \theta_I + \theta) \sinh(2r) \}. \quad (46)$$

To isolate the minima (maxima) of the CV we set the argument of the second cosine to π (0) by selecting appropriate $\theta_S(t)$ and $\theta_I(t)$ such that $\theta_S + \theta_I + \theta = \pi$ (0), where θ is the phase of the squeezing parameter given in Eq. (38). We thus obtain expressions for the maximum and minimum CV in the between the signal and idler modes of the RS:

$$\Delta_{S,I;\text{min}}^2 = (n_S^{\text{th}} + n_I^{\text{th}} + 1) e^{-2r}, \quad (47)$$

$$\Delta_{S,I;\text{max}}^2 = (n_S^{\text{th}} + n_I^{\text{th}} + 1) e^{2r}. \quad (48)$$

In Fig. 7 (b), we plot the time evolution of the squeezing amplitude, $r(\tilde{t})$ (orange), and the minimum and maximum of the correlation variance in the RS (black). As can be seen, the CV reaches a minimum value of ≈ 0.219 at time $\tilde{t} \approx 0.89$.

We now wish to calculate the correlation variance between a single-defect mode in the signal

CROW and one in the idler CROW. To accomplish this, we select the time, denoted \tilde{t}_0 and labeled in Fig. 7, at which $\Delta_{S,I;\min}^2$ is minimized. At this time, we retrieve the calculated quantities $r(\tilde{t}_0)$, $n_S^{\text{th}}(\tilde{t}_0)$, and $n_I^{\text{th}}(\tilde{t}_0)$, given in Table II, to define the density operator of the generated two-mode squeezed thermal state at the time \tilde{t}_0 according to Eq. (34). Note that, because we have designed the structure such that the signal and idler decay times are nearly equal and are much longer than the pump pulse duration in the RS, the number of thermal photons is very low and is much smaller than the total number of photons.

$r(\tilde{t}_0)$	$n_S^{\text{th}}(\tilde{t}_0)$	$n_I^{\text{th}}(\tilde{t}_0)$
0.6497	0.0458	0.0453
$\Delta_{S,I;\min}^2(\tilde{t}_0)$	$n_S(\tilde{t}_0)$	$n_I(\tilde{t}_0)$
0.219	18.3927	18.3867

TABLE II: Summary of parameters for the state generated in the RS at time $\tilde{t} = \tilde{t}_0$.

In the next section, we use this density operator as the starting point to compute the quantum evolution of the observables of interest in the signal and idler CROWs for times $\tilde{t} \geq \tilde{t}_0$. In doing this, we are assuming that the effect of the pump can be ignored for times $\tilde{t} > \tilde{t}_0$. This is a conservative approximation: Eqs. (39) and (42) show that the correlation variance will always be larger (worse) when no pump is present.

D. Correlation Variance in in the output CROWs

In the previous two subsections, we modeled the evolution of the pump light as it coupled into the RS and computed the density operator of the 2MSTS generated in the RS by the pump light. In this section, we model the free quantum evolution of the 2MSTS in the full system in the presence of loss but without the pump and compute the time-dependent expectation value of the CV between output CROW cavities. We accomplish this by first solving the adjoint master equation for the time-evolution

of the full-system QM ladder operators, and then use the initial state of the system at time $\tilde{t} = \tilde{t}_0$ to calculate time dependence of the photon number and correlation variance.

Consider now the CV between two cavities, one each in the signal and idler CROW n lattice sites away from their respective coupling cavity. We shall denote the n^{th} cavity in the signal and idler CROW as S_n and I_n respectively (see Fig. 1), and the CV between them as $\Delta(S_n, \tilde{t}_S; I_n, \tilde{t}_I)$, where we allow the measurement times \tilde{t}_S and \tilde{t}_I to be different. This CV may be expressed in terms of the quadrature operators in the two cavities as

$$\Delta(S_n, \tilde{t}_S; I_n, \tilde{t}_I) = \left\langle [X_{S_n}(\tilde{t}_S) - X_{I_n}(\tilde{t}_I)]^2 \right\rangle + \left\langle [Y_{S_n}(\tilde{t}_S) + Y_{I_n}(\tilde{t}_I)]^2 \right\rangle, \quad (49)$$

where

$$X_q(t) = \frac{1}{2}(a_q(t) + a_q^\dagger(t)), \quad (50)$$

$$Y_q(t) = \frac{1}{2i}(a_q(t) - a_q^\dagger(t)). \quad (51)$$

The task now is to determine the time evolution of the Heisenberg operators in Eqs. (50) and (51). In the previous subsection, we modeled the dynamics of the density operator for the light in the RS only. We first determine the evolution of the full-system QM ladder operators and then we express the single-defect QM ladder operators (the $a_q(t)$ -operators in Eqs. (50, 51)) in terms of the full-system QM ladder operators.

Due to the non-orthogonality of the basis of full-system QMs the non-Hermitian free Hamiltonian describing light in the full system takes the form [28]

$$H_{\text{free}} = \sum_{\mu=1}^N \hbar\tilde{\omega}_\mu b_\mu^\dagger c_\mu, \quad (52)$$

where $N = 184$ is the total number of full-system QMs which is equal to the number of

cavities, and the full-system QM ladder operators obey the following relations:

$$c_\mu = \sum_\nu P_{\mu\nu} b_\nu, \quad b_\mu = \sum_\nu O_{\mu\nu} c_\nu, \quad (53)$$

$$c_\mu^\dagger = \sum_\nu P_{\mu\nu}^* b_\nu^\dagger, \quad b_\mu^\dagger = \sum_\nu O_{\mu\nu}^* c_\nu^\dagger, \quad (54)$$

where \overleftrightarrow{P} is the inverse of \overleftrightarrow{O} of Eq. (12). The full-system QM ladder operators obey the commutation relations:

$$[c_\mu, b_\mu^\dagger] = \delta_{\mu\nu}, \quad (55)$$

$$[b_\mu, c_\nu^\dagger] = -\delta_{\mu\nu}, \quad (56)$$

$$[b_\mu, b_\nu^\dagger] = O_{\mu\nu}, \quad (57)$$

$$[b_\mu^\dagger, b_\nu^\dagger] = [c_\mu, c_\nu] = 0. \quad (58)$$

The state with a single photon in the μ^{th} full-system QM is created by the rightwards action of b^\dagger on the vacuum, which is an eigenstate of the linear Hamiltonian of Eq. (52). We can construct the full-system QM ladder operators in terms of the single-cavity QM ladder operators following Eq. (4):

$$b_\mu^\dagger = \sum_q v_{q\mu} a_q^\dagger, \quad b_\mu = \sum_q v_{q\mu}^* a_q. \quad (59)$$

Inverting Eq. (59) yields the inverse relations

$$a_q^\dagger = \sum_\mu w_{\mu q} b_\mu^\dagger, \quad a_q = \sum_\mu w_{\mu q}^* b_\mu. \quad (60)$$

Below, we shall write the time-dependent photon number and correlation variance in terms of the a -operators. First, though, we must determine the time-evolution of the c -operators, since, as we shall see, it is these (and not the b -operators) that display simple single-frequency time-dependence. We begin with the adjoint master equation, which describes the

time-evolution of a Heisenberg picture operator A_H in terms of the free Hamiltonian in Eq. (52) [30]:

$$\frac{dA_H}{d\tilde{t}} = -\frac{i}{\hbar} A_H H_{\text{free}} + \frac{i}{\hbar} H_{\text{free}}^\dagger A_H + i \sum_\mu (\tilde{\omega}_\mu b_\mu^\dagger A_H c_\mu - \tilde{\omega}_\mu^* c_\mu^\dagger A_H b_\mu). \quad (61)$$

Taking $A_H \rightarrow c_\nu$ we obtain, after some algebra,

$$c_\nu(\tilde{t}) = c_\nu e^{-i\tilde{\omega}_\nu(\tilde{t}-\tilde{t}_0)}, \quad (62)$$

where $c_\nu \equiv c_\nu(\tilde{t}_0)$, displaying the simple behavior we expected. For $c^\dagger(\tilde{t})$ we simply take the Hermitian conjugate of Eq. (62). More generally, it is easy to show that for any normally-ordered set of c -operators, the evolution of each operator is simply given by the result shown in Eq. (62). The time-evolution of the b_ν 's is found via construction from the c_ν 's to be [28]

$$b_\mu(\tilde{t}) \equiv \sum_{\nu=1}^N O_{\nu\mu} c_\nu(\tilde{t}), \quad (63)$$

where again $b^\dagger(\tilde{t})$ is obtained via the Hermitian conjugate of Eq. (63). The time-evolution of the single-cavity QM operators (the a -operators), obtained using Eqs. (60), (62), and (63), is found to be

$$\vec{a}(\tilde{t}) = \overleftrightarrow{W} \overleftrightarrow{O} \overleftrightarrow{F}(\tilde{t}) \overleftrightarrow{P} \overleftrightarrow{V} \vec{a} \quad (64)$$

$$= \overleftrightarrow{\Phi}(\tilde{t}) \vec{a}, \quad (65)$$

where $\vec{a} \equiv (a_1, a_2, \dots, a_p)^T$ and $\overleftrightarrow{F}(\tilde{t}) = \text{diag}(e^{-i\tilde{\omega}_1(\tilde{t}-\tilde{t}_0)}, e^{-i\tilde{\omega}_2(\tilde{t}-\tilde{t}_0)}, \dots, e^{-i\tilde{\omega}_p(\tilde{t}-\tilde{t}_0)})$.

Inserting Eq. (65) into Eqs. (50, 51) and substituting the result into Eq. (49) yields, after some algebra

$$\begin{aligned} \Delta^2(S_n, \tilde{t}_S; I_n, \tilde{t}_I) &= \frac{1}{2}(B_{S_n S_n} + B_{I_n I_n}) + \sum_{m, m'=1}^N [\phi_{S_{nm}}^*(\tilde{t}_S) \phi_{S_{nm'}}(\tilde{t}_S) + \phi_{I_{nm}}^*(\tilde{t}_I) \phi_{I_{nm'}}(\tilde{t}_I)] \langle a_m^\dagger a_{m'} \rangle \\ &\quad - 2 \operatorname{Re} \left\{ \sum_{m, m'=1}^N \phi_{S_{nm}}(\tilde{t}_S) \phi_{I_{nm'}}(\tilde{t}_I) \langle a_m a_{m'} \rangle \right\}. \end{aligned} \quad (66)$$

In Eq. (66), all the time-dependence is contained within the $\phi_{pq}(\tilde{t})$ elements, and the only quantities still unknown are the $\langle a_p^\dagger a_q \rangle$ and $\langle a_p a_q \rangle$ ensemble averages, which we shall now compute. These ensemble averages are evaluated at the time $\tilde{t} = \tilde{t}_0$ (see Fig. 7). We assume that at this time, the only light in the system is the generated light which exists exclusively in the signal and idler QMs of the RS. This enables us to write:

$$\langle a_p a_q \rangle = \sum_{j, k} \sigma_{pj}^* \sigma_{qk}^* \langle d_j d_k \rangle, \quad (67)$$

$$\langle a_p^\dagger a_q \rangle = \sum_{j, k} \sigma_{pj} \sigma_{qk}^* \langle d_j^\dagger d_k \rangle, \quad (68)$$

where p and q are now cavities in the RS, the d_j (d_j^\dagger) are the annihilation (creation) operators for the j^{th} RS QM, and the σ_{pj} are the matrix elements of the matrix $\overset{\leftrightarrow}{\Sigma} = \overset{\leftrightarrow}{U} \overset{\leftrightarrow{-1}}{U}$ (see Eq. (15)). In Eqs. (67-68), j and k run through only the signal ($j = S$) and idler ($k = I$) modes of the

$$\langle a_p a_q \rangle = -(\sigma_{pS}^* \sigma_{qI}^* + \sigma_{pI}^* \sigma_{qS}^*) (n_S^{th} + n_I^{th} + 1) e^{i\theta} \cosh r, \sinh r, \quad (74)$$

$$\langle a_p^\dagger a_q \rangle = \sigma_{pS} \sigma_{qS}^* (n_S^{th} \cosh^2 r + (1 + n_I^{th}) \sinh^2 r) + \sigma_{pI} \sigma_{qI}^* (n_I^{th} \cosh^2 r + (1 + n_S^{th}) \sinh^2 r). \quad (75)$$

Finally, the combination of Eqs. (74, 75) with Eq. (66) yields an expression for the correlation variance between two cavities in the signal and idler output CROWs. The preceding analysis also yields an expression for the average photon number in the output CROW cavities: since Eq. (75) is normally ordered we may simply use Eq.

RS.

We now directly evaluate the ensemble averages in Eqs. (67-68) for use in the next two sections. Using the density operator from Eq. (34), the ensemble average for a general operator A , acting on a two-mode squeezed state can be expressed as:

$$\begin{aligned} \langle A \rangle &= \operatorname{Tr}\{A\rho\} \\ &= \operatorname{Tr}\left\{A S_2(\xi) \rho^{\text{th}} S_2^\dagger(\xi)\right\} \\ &= \operatorname{Tr}\left\{S_2^\dagger(\xi) A S_2(\xi) \rho^{\text{th}}\right\}. \end{aligned} \quad (69)$$

Using the standard relations [39], we obtain:

$$S_2^\dagger(\xi) d_S S_2(\xi) = d_S \cosh r - d_I^\dagger e^{i\theta} \sinh r, \quad (70)$$

$$S_2^\dagger(\xi) d_I S_2(\xi) = d_I \cosh r - d_S^\dagger e^{i\theta} \sinh r, \quad (71)$$

$$S_2^\dagger(\xi) d_S^\dagger S_2(\xi) = d_S^\dagger \cosh r - d_I e^{-i\theta} \sinh r, \quad (72)$$

$$S_2^\dagger(\xi) d_I^\dagger S_2(\xi) = d_I^\dagger \cosh r - d_S e^{-i\theta} \sinh r. \quad (73)$$

Thus, from Eq. (69) and Eqs. (70 - 73), we can evaluate Eqs. (67, 68). After some algebra, we obtain:

(65) to write

$$\langle a_n^\dagger a_n \rangle(t) = \sum_{q \in RS} \phi_{q,n}^*(t) \phi_{q,n}(t) \langle a_q^\dagger a_q \rangle. \quad (76)$$

In the next section, we present and discuss the solutions to Eqs. (66) and (76).

IV. RESULTS

In this section we present the results obtained for the PC CCS in Fig. 1 using our theoretical approach. In particular, we present the time evolution of the average photon number and correlation variance in cavities in the three CROWS. We begin by examining the time-dependent average photon number in cavities in the three CROWS to ascertain the spatio-temporal dynamics of the generated light. Next we compute the time-dependent correlation variance between light in the signal and idler CROWS by solving Eq. (66). We will explore a variety of pumping configurations and time delays to demonstrate the utility of our approach and the performance of our coupled cavity system.

A. Photon Number

We begin by using Eq. (76) to calculate the time dependence of the photon number for the first few cavities in each of the three CROWS for the pump pulse that was used to produce the results presented in Fig. 7. The photons we study when computing the time-dependent photon number here are the generated photons, which exist in a multimode entangled squeezed thermal state in the QMs of the full system.

In Fig. 8, we plot the photon number in select cavities in the three CROWS as a function of time. In the signal and idler CROWS, the photon number in a given cavity exhibits a series of peaks that decrease in amplitude with time. The time that the first peak arrives in each cavity increases, and its amplitude decreases as the distance of the cavity from the RS increases. This is simply due to the effects of the group velocity and scattering loss, respectively. One might expect that the period between successive peaks in the CROWS to be given by the beat period between the signal and idler modes in the RS. This is approximately the case in the pump CROW. However, complications arising from the reflections off of the CROWS and the coupling cavities results in the oscillation period

in the signal and idler CROWS being closer to twice the beat period.

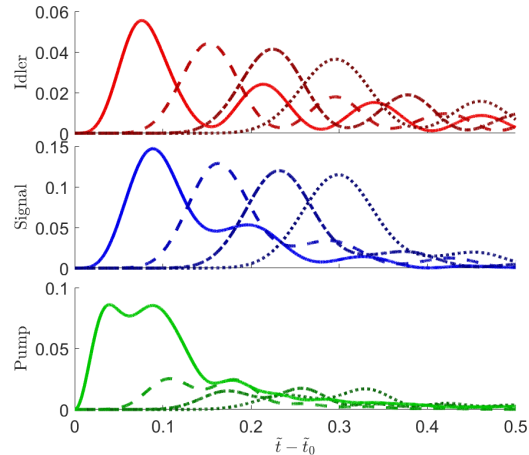


FIG. 8: Average photon number in the 1st (solid), 4th (dash), 7th (dash-dot), and 10th (dot) cavities of the idler, signal, and pump CROWS as a function of time. The labeling of the cavities is given in Fig. 1. Note that the photon numbers do not include the input pump pulse photons, but rather the photons generated in the RS.

Another feature seen in Fig. 8, which is pertinent to the following analysis of the CROW CV, is the difference in the propagation speeds in the signal and idler CROWS. Each of the CROWS is designed to carry light at its band center. However, due to the difference in inter-cavity coupling in each of the CROWS, the group velocity at band center is different in each of the CROWS. We infer this from Fig. 2, where the bandwidths of the three CROWS are different, and so the group velocities at band center are different. Indeed, we see that the average photon number peaks earlier in the first idler cavity than the first signal cavity, though by cavity 13 the signal light begins arriving first. This phenomenon is clearly seen in Fig. 9, where we plot the photon number in three different cavities in the signal and idler CROWS as a function of time.

From Fig. 8, we also see that for cavities

sufficiently far from the RS, most of the generated light is in the signal and idler waveguides, as desired. However, at early times, a substantial fraction of the generated light is in the pump CROW cavities close to the RS. Most of this light cannot propagate down the pump CROW because its frequency is outside of the pass-band of the pump CROW (see Fig. 2). Thus, it evanescently decays and its amplitude is very small beyond the third cavity in the pump CROW. The relatively large number of generated photons in the cavities of the pump CROW that are close to the RS arises due to the strong coupling of the pump CROW to the RS. We have deliberately chosen this coupling to be strong to reduce the residence time of the pump light in the RS; in studying this system and others similar to it we have found that a shorter residence time limits the generation of thermal noise from scattering loss during the nonlinear process in the RS.

Finally, we observe from Fig. 8 that there are more photons in the signal CROW than in the idler CROW. There are two different contributors to this imbalance. The first is the result of the different coupling strengths between the RS and the signal and idler CROWs. Since the intrinsic Q s of the signal and idler RS QMs were different, the coupling between these QMs and their respective CROWs had to be tuned separately so as to achieve the same loaded Q for the signal and idler RS modes. This was accomplished via the coupling cavities indicated in Fig. 1. Manipulating the loaded Q s of the RS QMs in this manner resulted in a difference in the out-coupling rate between the signal and idler modes. Ideally the loaded Q s and the out-coupling efficiency of the signal and idler RS QMs would be approximately equal, but it was not possible to achieve this for this structure, while also keeping the equal frequency spacing between the modes. The second contributor to the imbalance in the signal and idler photon number is the effect of the strongly-coupled pump CROW, which results in a more complicated time evolution of the generated light after the pump has left. Indeed, when we perform the same analysis but con-

sider a system with the pump CROW removed, the time-dependent photon numbers in the signal and idler CROWs are nearly equal.

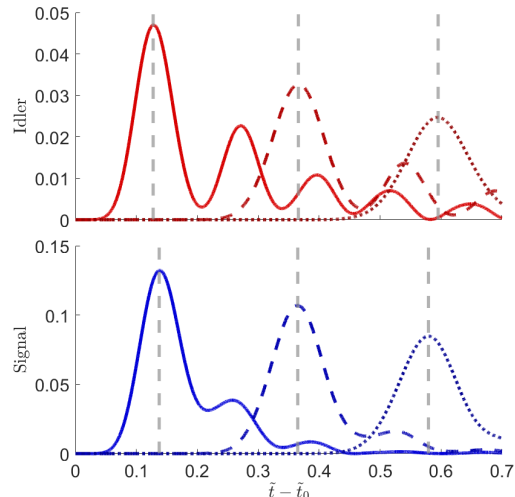


FIG. 9: Photon numbers in the 3rd (solid), 13th (dashed), and 23rd (dotted) signal and idler CROW cavities as a function of time. Note that the signal light overtakes the idler when they reach the 13th cavities in the CROWs. Vertical dashed lines indicate the pulse peaks.

B. Correlation Variance

We now turn our attention to evaluating the correlation variance between signal and idler CROW cavities as expressed in Eq. (66). We once again use the pulse shown in Fig. 7. For simplicity, we shall first set $t_S = t_I$ in Eq. (66). The CV expression in Eq. 66 includes rapidly oscillating terms modulated by a slowly varying envelope. Experimentally, these fast oscillations will be removed during a heterodyne measurement by locking the measurement phase with the local oscillators. Thus for simplicity in Fig. 10 we plot only the slowly varying upper and lower bounding envelopes of the CV function. The lower bound of the envelope is a measure of inseparability of the state: the state is inseparable if this lower bound of the CV is less

than unity. We see from Fig. 10 that in the $n = 5$ cavity pair, the CV falls to about 0.93. Moreover, entanglement between pairs of cavities persists for cavities that are more than $40d = 57.6 \mu\text{m}$ away from the coupling cavities.

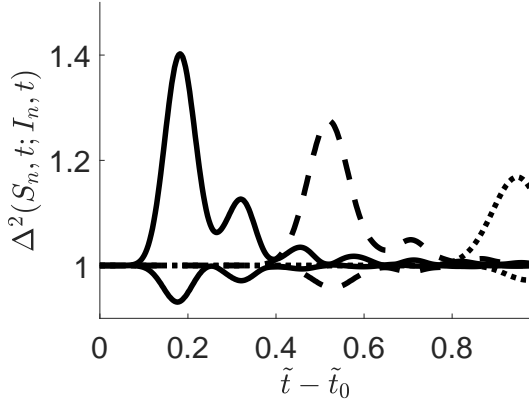


FIG. 10: Envelope of the CV between pairs of signal and idler CROW cavities as a function of time. The fast oscillations that arise in the CV have been omitted for clarity and only the envelope has been plotted. Curves shown are for the 5th (solid), 20th (dashed), and 40th (dotted) pairs away from the coupling cavities.

In Fig. 11, we plot the global minima and maxima of the CV envelopes from the first 50 output CROW cavity pairs with $\tilde{t}_S = \tilde{t}_I$. The minima of the CV remain below unity in all cases, demonstrating entanglement far from the RS. To highlight the importance of taking into account the QM non-orthogonality in complicated PC CCSs (see Fig. (5)), we have repeated the calculation ignoring the non-orthogonality, *i.e.*, setting $\vec{O} = \vec{I}$ in Eq. (65), and present the results for the CV envelope as the dashed lines in Fig. 11. Note that for cavities close to the RS, the difference between the CV minimum and unity can change by up to 16%, indicating that it is important to include the nonorthogonality of the modes in the calculations for this system.

We now consider the effects of varying the pump pulse energy and width in k -space on the

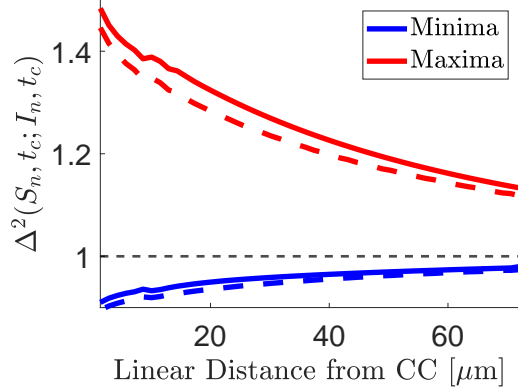


FIG. 11: Minimum and maximum of the CV envelope for pairs of output CROW cavities as a function of distance the coupling cavity (CC). Dashed lines show the results obtained assuming that the system QMs are orthogonal.

CV and the optimal measurement times. Although the naïve choice of $\tilde{t}_S = \tilde{t}_I$ in Eq. (66) is satisfactory for low pump energies, the increased thermal noise that is generated as the pump energy increases eventually forces one to alter the measurement times to account for the group velocity difference in the presence of this increased noise. To demonstrate this, we calculated the CV between the $n = 3$ cavities in the signal and idler CROWS under a variety of pumping configurations and measurement times. In what follows, we fix \tilde{t}_S and define the measurement delay time as $\tilde{\tau} = \tilde{t}_S - \tilde{t}_I$.

In Fig. 12, we plot the minimum and maximum CV as a function of κ^{-1} for a fixed pump energy of 670 fJ for fourteen different $\tilde{\tau}$, from $\tilde{\tau} = 0$ to $\tilde{\tau} = 0.065\Gamma_+$ in increments of $0.005\Gamma_+$. Note that the minimum CV initially increases and then decreases as $\tilde{\tau}$ is increased, while the maximum CV monotonically decreases. The effect of varying κ between $2\pi/15d$ and $2\pi/45d$ is less pronounced than that of varying the measurement time delay $\tilde{\tau}$. Specifically, with a fixed pump energy of 670 fJ (as in Fig. 12), we find that choosing $0.045\Gamma_+ \leq \tilde{\tau} \leq 0.065\Gamma_+$ (the darkest six curves) greatly reduces the depen-

dence of the CV minimum on $1/\kappa$, while also reducing the CV maximum. From an alternative perspective, if the optimum $\tilde{\tau}$ is chosen to minimize the CV minimum, then the frequency width (and thus the temporal width) of the pump pulse may be adjusted to minimize the CV maximum, which has little effect on the CV minimum.

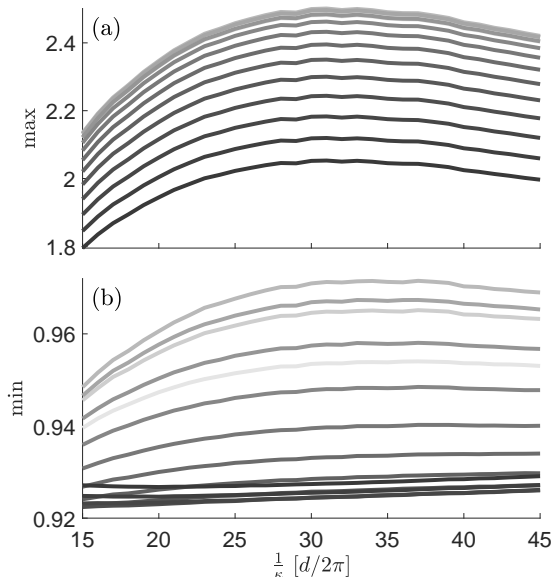


FIG. 12: Minimum and maximum of the CV for the $n = 3$ signal and idler cavities as a function of $1/\kappa$, with a fixed pump energy of 670 fJ. Each curve corresponds to a particular choice of $\tilde{\tau}$ from $\tilde{\tau} = 0$ (lightest curve) to $\tilde{\tau} = 0.065\Gamma_+$ (darkest curve) in increments of $0.005\Gamma_+$.

In Fig. 13, we plot the minimum and maximum CV as a function of pump energy for a fixed $\kappa = 2\pi/20d$. The pump energy has a more pronounced effect on the CV extrema than κ . Fig. 13 (b) shows that once the pump energy exceeds ≈ 1 pJ, the entanglement vanishes unless the time-delay is sufficiently increased [40]. From Fig. 13 (a), we see that for pulse energies above ≈ 1 pJ, the CV maximum exhibits an exponential dependence on the pump energy: although entanglement may be recovered with an appropriate choice of $\tilde{\tau}$, the large increase in the

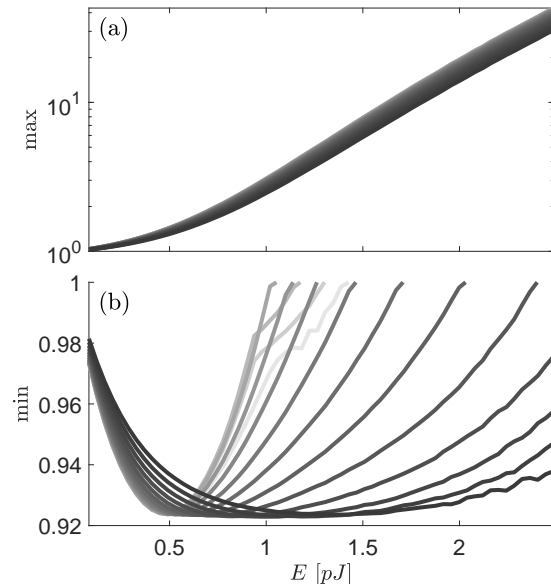


FIG. 13: CV for the $n = 3$ signal and idler cavities as a function of pump energy with $\kappa = 2\pi/20d$ fixed. Each curve corresponds to a particular choice of $\tilde{\tau}$ from $\tilde{\tau} = 0$ (lightest curve) to $\tilde{\tau} = 0.065\Gamma_+$ (darkest curve) in increments of $0.005\Gamma_+$.

CV maximum makes these higher pulse energies undesirable. We find that a good configuration that gives a low minimum CV, while keeping the pulse energy and the maximum CV modest, is as follows: a pump pulse energy of ≈ 670 fJ, $\kappa = 2\pi/20d$, and $\tilde{\tau} = 0.45\Gamma_+$. This gives a minimum and maximum CV for the $n = 3$ cavity pair of 0.923 and 1.74 respectively.

V. CONCLUSION

We have presented a four-step theoretical approach to simulate the generation and propagation dynamics of a quantum state of light in lossy nanophotonic structures consisting of coupled open optical resonators. Using our theoretical approach, we designed a PC CCS for the generation of entangled 2MSTS of light on-chip and computed the time-dependent photon num-

ber and correlation variance in the electric field of this state at various points in space and time in the PC CCS. We used as a basis for our analysis the 184 leaky QMs of the full system, which were computed with a tight-binding approach. Our analysis showed that the RS, when excited with a Gaussian pump pulse carrying an initial energy between 0.5 and 1 pJ and a k -space width between $2\pi/15d$ and $2\pi/45d$, generates a two-mode squeezed thermal state, which exits the RS as two spatially separated pulses of light that remain entangled as they propagate.

We find that although the nonlinear generation process creates strong squeezing and low thermal photon noise in the RS, the squeezing degrades substantially after transmission into the output CROWs. The difference between the intrinsic quality factors of the RS QMs and the over-coupling of the pump CROW contribute to this degradation. Thus, it is clear that further refinement of the design of the RS and coupling to the CROWs in this system is required to balance the number of photons going into each of the CROWs, while keeping the loaded cavity Qs in the desired range.

Our analysis of the CV demonstrates the ability of our theoretical approach to efficiently and accurately calculate the generation and evolution of quantum states of light in coupled-cavity systems. The efficiency of our approach allows us to evaluate many pumping schemes and ascertain the effect of changes to the pump, or changes to any individual cavities in the system, at every stage of the process.

Although we focused on the time-dependent photon number and CV in this work, our method is general and can be applied to any observable which can be expanded in terms of the full-system QMs. The general procedure applied here may also be extended to any nanophotonic system composed of coupled elements whose modes are easily obtained. This approach is particularly useful when combining simple elements causes the entire system to lose the properties which allowed for efficient computation of the modes of the constituents.

Possible extensions of the theoretical approach presented here include the handling of

other device types, such as line-defect waveguides, and a relaxation of the undepleted pump approximation. Other applications of the theoretical approach presented here include designing structures for the on-chip generation of larger numbers of entangled states, including cluster states and non-Gaussian states, designing implementations of quantum gates on-chip, and studying the dynamics of quantum information protocols in the presence of loss.

ACKNOWLEDGMENTS

This work was supported by The Canadian Foundation for Innovation and the Natural Sciences and Engineering Research Council of Canada.

-
- [1] O. Pfister, Continuous-variable quantum computing in the quantum optical frequency comb, *Journal of Physics B: Atomic, Molecular and Optical Physics* **53**, 012001 (2020).
- [2] G. Adesso, S. Ragy, and A. R. Lee, Continuous variable quantum information: Gaussian states and beyond, arXiv: 1401.4679 (2014).
- [3] K. A. et al., A manufacturable platform for photonic quantum computing, arXiv: 2404.17570 (2024).
- [4] M. Feldman, T. Volkoff, Z. Holmes, S. Hong, C. Marvinney, R. Pooser, A. Sornborger, and A. M. Marino, A continuous variable quantum compiler (CLEO, Charlotte, 2024) p. FM1K.2.
- [5] N. C. Menicucci, P. V. Loock, M. Gu, C. Weedbrook, T. C. Ralph, and M. A. Nielsen, Universal quantum computation with continuous-variable cluster states, *Physical Review Letters* **97**, 110501 (2006).
- [6] A. Leverrier and P. Grangier, Continuous-variable quantum-key-distribution protocols with a non-gaussian modulation, *Physical Review A* **83**, 42312 (2011).
- [7] K. E. Dorfman, F. Schlawin, and S. Mukamel, Nonlinear optical signals and spectroscopy with quantum light, *Reviews of Modern Physics* **88**, 045008 (2016).
- [8] T. L. S. Collaboration, A gravitational wave observatory operating beyond the quantum shot-noise limit, *Nature Physics* **7**, 962 (2011).
- [9] R. Schnabel, Squeezed states of light and their applications in laser interferometers (2017).
- [10] H. Tomoda, A. Machinaga, K. Takase, J. Harada, T. Kashiwazaki, T. Umeki, S. Miki, F. China, M. Yabuno, H. Terai, D. Okuno, and S. Takeda, Boosting the generation rate of squeezed single-photon states by generalized photon subtraction, *Phys. Rev. A* **110**, 033717 (2024).
- [11] H. Seifoory, S. Doutre, M. M. Dignam, and J. E. Sipe, Squeezed thermal states: the result of parametric down conversion in lossy cavities, *Journal of the Optical Society of America B* **34**, 1587 (2017).
- [12] C. Vendromin and M. M. Dignam, Optimization of a lossy microring resonator system for the generation of quadrature-squeezed states, *Physical Review A* **102**, 023705 (2020).
- [13] L. S. M. et al., Quantum computational advantage with a programmable photonic processor, *Nature* **606**, 75 (2022).
- [14] J. W. Silverstone, R. Santagati, D. Bonneau, M. J. Strain, M. Sorel, J. L. O'Brien, and M. G. Thompson, Qubit entanglement between ring-resonator photon-pair sources on a silicon chip, *Nature Communications* **6**, 7948 (2015).
- [15] K. Tan, M. Menotti, Z. Vernon, J. E. Sipe, M. Liscidini, and B. Morrison, Stimulated four-wave mixing in linearly uncoupled resonators, *Opt. Lett.* **45**, 873 (2020).
- [16] Y. Zhang, M. Menotti, K. Tan, V. D. Vaidya, D. H. Mahler, L. G. Helt, L. Zatti, M. Liscidini, B. Morrison, and Z. Vernon, Squeezed light from a nanophotonic molecule, *Nature Communications* **12**, 2233 (2021).
- [17] N. Quesada, L. G. Helt, M. Menotti, M. Liscidini, and J. E. Sipe, Beyond photon pairs: Nonlinear quantum photonics in the high-gain regime, arXiv: , 2110.04340 (2021).
- [18] A. Mataji-Kojouri and M. Liscidini, Spontaneous four-wave mixing in a sequence of lossy ring resonators, *Physical Review A* **110**, 043509 (2024).
- [19] C. Vendromin and M. M. Dignam, Continuous-variable entanglement in a two-mode lossy cavity: An analytic solution, *Physical Review A* **103**, 022418 (2021).
- [20] C. Vendromin and M. M. Dignam, Simple way to incorporate loss when modeling multimode-entangled-state generation, *Physical Review A* **105**, 063707 (2022).
- [21] C. Vendromin, J. E. Sipe, and M. Liscidini, Programmable integrated source of polarization and frequency-bin hyperentangled photon pairs, *Physical review. A* **111** (2025).
- [22] C. Vendromin, Y. Liu, Z. Yang, and J. E. Sipe, Highly squeezed states in ring resonators: Beyond the undepleted-pump approximation, *Physical Review A* **110**, 033709 (2024).
- [23] M. K. Dezfouli and M. M. Dignam, Photon-pair generation in lossy coupled-resonator optical waveguides via spontaneous four-wave mixing, *Physical Review A* **95**, 033815 (2017).
- [24] H. Seifoory and M. M. Dignam, Squeezed-state evolution and entanglement in lossy coupled-resonator optical waveguides, *Physical Review A* **97**, 023840 (2018).
- [25] H. Seifoory, L. G. Helt, J. E. Sipe, and M. M. Dignam, Counterpropagating continuous-variable entangled states in lossy

- coupled-cavity optical waveguides, *Physical Review A* **100**, 033839 (2019).
- [26] H. Seifoory, Z. Vernon, D. H. Mahler, M. Menotti, Y. Zhang, and J. E. Sipe, Degenerate squeezing in a dual-pumped integrated microresonator: Parasitic processes and their suppression, *Physical Review A* **105**, 033524 (2022).
- [27] D. P. Fussell and M. M. Dignam, Quasimode-projection approach to quantum-dot-photon interactions in photonic-crystal-slab coupled-cavity systems, *Phys. Rev. A* **77**, 053805 (2008).
- [28] M. M. Dignam and M. K. Dezfouli, Photon-quantum-dot dynamics in coupled-cavity photonic crystal slabs, *Physical Review A - Atomic, Molecular, and Optical Physics* **85**, 013809 (2012).
- [29] D. P. Fussell and M. M. Dignam, Engineering the quality factors of coupled-cavity modes in photonic crystal slabs, *Applied Physics Letters* **90**, 183121 (2007).
- [30] M. K. Dezfouli, M. M. Dignam, M. J. Steel, and J. E. Sipe, Heisenberg treatment of pair generation in lossy coupled-cavity systems, *Physical Review A - Atomic, Molecular, and Optical Physics* **90**, 043832 (2014).
- [31] A. Yariv, Y. Xu, R. K. Lee, and A. Scherer, Coupled-resonator optical waveguide: a proposal and analysis, *Opt. Lett.* **24**, 711 (1999).
- [32] J. D. Joannopolous, S. G. Johnson, J. N. Winn, and R. D. Meade, *Photonic crystals : molding the flow of light*, 2nd ed. (Princeton University Press, Princeton, 2008).
- [33] See <https://www.ansys.com/products/optics/fdtd#tab1-1>. Simulation parameters available upon request.
- [34] J. E. Sipe, Photons in dispersive dielectrics, *Journal of Optics A: Pure and Applied Optics* **11**, 114006 (2009).
- [35] M. Dinu, F. Quochi, and H. Garcia, Third-order nonlinearities in silicon at telecom wavelengths, *Applied Physics Letters* **82**, 2954 (2003).
- [36] A. D. Bristow, N. Rotenberg, and H. M. V. Driel, Two-photon absorption and kerr coefficients of silicon for 850-2200 nm, *Applied Physics Letters* **90**, 191104 (2007).
- [37] The second line is approximate since in the previous line we use ϵ_{RS} , while \overleftrightarrow{B} was computed using ϵ .
- [38] L. Duan, G. Giedke, J. Cirac, and P. Zoller, Inseparability criterion for continuous variable systems, *Physical Review Letters* **84**, 2722 (2000).
- [39] C. C. Gerry and P. Knight, *Introductory quantum optics* (Cambridge University Press, Cambridge, UK, 2005).
- [40] The jogs in the CV minima in the lighter curves are caused by secondary peaks becoming more inseparable than the initial pulse for high enough pump energy.